

TIME-DEPENDENT TURBULENT HEATING OF OPEN FLUX TUBES IN THE CHROMOSPHERE, CORONA, AND SOLAR WIND

L. N. WOOLSEY¹ AND S. R. CRANMER^{1,2}

Draft version September 2, 2015

ABSTRACT

We investigate several key questions of plasma heating in open-field regions of the corona that connect to the solar wind. We present results for a model of Alfvén-wave-driven turbulence for three typical open magnetic field structures: a polar coronal hole, an open flux tube neighboring an equatorial streamer, and an open flux tube near a strong-field active region. We compare time-steady, one-dimensional turbulent heating models (Cranmer et al. 2007) against fully time-dependent three-dimensional reduced-magnetohydrodynamics modeling of BRAID (van Ballegooijen et al. 2011). We find that the time-steady results agree well with time-averaged results from BRAID. The time-dependence allows us to investigate the variability of the magnetic fluctuations and of the heating in the corona. The high-frequency tail of the power spectrum of fluctuations forms a power law whose exponent varies with height, and we discuss the possible physical explanation for this behavior. The variability in the heating rate is bursty and nanoflare-like in nature, and we analyze the amount of energy lost via dissipative heating in transient events throughout the simulation. The average energy in these events is $10^{21.91}$ erg, within the “picoflare” range, and many events reach classical “nanoflare” energies. We also estimated the multithermal distribution of temperatures that would result from the heating-rate variability, and found good agreement with observed widths of coronal differential emission measure (DEM) distributions. The results of the modeling presented in this paper provide compelling evidence that turbulent heating in the solar atmosphere by Alfvén waves accelerates the solar wind in open flux tubes.

1. INTRODUCTION

The solar atmosphere is characterized by a temperature profile that has puzzled scientists for decades. The photosphere, the visible surface of the Sun, is roughly 6000 K, while the diffuse corona above it is heated to millions of degrees. Observations have not been able to determine the mechanism(s) responsible for the extreme coronal heating, though many physical processes have been suggested. The same processes that might explain the temperature of the corona can also account for the acceleration of the solar wind. Only a small fraction of the mechanical energy in the Sun’s sub-photospheric convection zone needs to be converted to heat in order to power the corona. However, it has proved exceedingly difficult to distinguish between competing theoretical models using existing observations. Recent summaries of these problems and controversies have been presented by, e.g., Parnell & De Moortel (2012), McIntosh (2012), Klimchuk (2015), and Cranmer et al. (2015).

If solar wind flux tubes are open to interplanetary space, and if they remain open on timescales comparable to the time it takes plasma to accelerate into the corona, then the main sources of energy must be injected at the footpoints of the flux tubes. Thus, in wave/turbulence-driven models, the convection-driven jostling of the flux-tube footpoints is assumed to generate wave-like fluctuations that propagate up into the extended corona. These waves (usually Alfvén waves) are often proposed to partially reflect back down toward the Sun, develop into strong magnetohydrodynamic (MHD) turbulence, and dissipate gradually. In this project,

we use two models in this regime, ZEPHYR (Cranmer et al. 2007) and BRAID (van Ballegooijen et al. 2011). These and other such models have been shown to naturally produce realistic fast and slow winds with wave amplitudes of the same order of magnitude as those observed in the corona and heliosphere (see also Hollweg 1986; Matthaeus et al. 1999; Suzuki & Inutsuka 2006; Ofman 2010; Verdini et al. 2010; Chandran et al. 2011; Lionello et al. 2014; Matsumoto & Suzuki 2014; Woolsey & Cranmer 2014).

However, between the above ideas and others that claim reconnection plays the primary role in heating, nothing has been ruled out because (1) we have not yet made the observations needed to distinguish between the two paradigms, and (2) most models still employ free parameters that can be adjusted to improve the agreement with existing observational constraints. A complete solution must account for all important sources of mass and energy into the three-dimensional and time-varying corona. Regardless of whether the dominant coronal fluctuations are wave-like or reconnection-driven, they are generated at small spatial scales in the lower atmosphere and are magnified and “stretched” as they propagate up in height. Their impact on the solar wind’s energy budget depends crucially on the multi-scale topological structure of the Sun’s magnetic field.

The current generation of time-steady 1D turbulence-driven solar wind models (e.g. Cranmer et al. 2007; Verdini et al. 2010; Chandran et al. 2011; Cranmer et al. 2013a; Lionello et al. 2014) contain detailed descriptions of many physical processes relevant to coronal heating and solar wind acceleration. However, none of them self-consistently simulate the actual process of MHD turbulent cascade as a consequence of the partial reflections and nonlinear interactions of Alfvénic wave packets. Thus, it is important to improve our understanding of the flux-tube geometry of the open-field corona and how various types of fluctuations interact with those

lwoolsey@cfa.harvard.edu

¹ Harvard-Smithsonian Center for Astrophysics, 60 Garden St., Cambridge, MA 02138, USA

² Department of Astrophysical & Planetary Sciences, University of Colorado, Boulder, CO 80309, USA

structures by using higher-dimensional and time-dependent models to understand the underlying physical processes.

In Section 2, we describe the modeling used to improve our understanding of the geometry of flux tubes in a time-steady sense and extending such understanding to time-dependent three-dimensional modeling. We focus on three models that are typical of common structures in the solar corona and present results of each in Section 3 and compare the one-dimensional, time-steady results from earlier work using ZEPHYR with the new three-dimensional, time-dependent results. We then analyze the polar coronal hole BRAID model further in Section 4. We include a discussion and conclusions in Section 5.

2. MHD TURBULENCE SIMULATION METHODS

2.1. Previous time-steady modeling

The magnetic field profiles used for this project are listed in Table 1 and are representative of a polar coronal hole, an equatorial streamer, and a flux tube neighboring an active region. The radial profiles of magnetic field strength $B(r)$ for these models are shown in Figure 1a (see also Banaszkiewicz et al. 1998; Cranmer et al. 2007). The Alfvén travel time from the base of the model to a height of 2 solar radii is calculated using Equation (3), and the expansion factor is defined by Wang & Sheeley (1990). The expansion factor is a ratio of the magnetic field strength at a height of 1.5 solar radii to the field strength at the photospheric base (here, at a height of 0.04 solar radii, the size of a supergranule), normalized such that an expansion factor of 1 is simple radial expansion, and an expansion factor larger than 1 is considered “superradial” expansion. Key results from these three models using ZEPHYR, a one-dimensional time-steady code introduced by Cranmer et al. (2007), are presented in Figure 1.

The polar coronal hole model has the smallest expansion from the photosphere to the low corona, and the highest wind speed at 1 AU. This relationship was first seen in empirical fits to observations (see, e.g., Wang & Sheeley 1990; Arge & Pizzo 2000) and has also been seen in models (see, e.g., Woolsey & Cranmer 2014). The equatorial streamer model represents an open flux tube directly neighboring the helmet streamers seen around the equator at solar minimum, and produces slower wind at 1 AU. The flux tube neighboring an active region has a stronger magnetic field above the transition region and an even slower wind speed at 1 AU than the equatorial streamer model. In these models, the transition region for PCH and EQS is at a height of 0.01 solar radii, and the NAR model has a transition region slightly higher, at a height of 0.015 solar radii. The density profiles were determined self-consistently with the wind speed using mass flux conservation.

ZEPHYR solves for a steady state solution to the solar wind properties generated by a one-dimensional open flux tube. By solving the equations of mass, momentum, and energy conservation and iterating to a stable solution, the code produces solar wind with mean properties that match observations and *in situ* measurements (Cranmer et al. 2007; Woolsey & Cranmer 2014). The code’s expression for the turbulent heating is a phenomenological cascade rate whose form has been guided and validated by several generations of numerical simulations and other models of imbalanced, reflection-driven turbulence (see, e.g., Hossain et al. 1995; Lithwick et al. 2007; Chandran et al. 2009; Oughton et al. 2015). For additional details, see Section 3.2 below.

ZEPHYR can only take us so far, however. It is only by modeling the fully 3D spatial and time dependence of the cascade process (together with the intermittent development of magnetic islands and current sheets on small scales) that we can better understand the way in which the plasma is heated by the dissipation of turbulence. We therefore make use of the time-dependent modeling of coronal turbulence introduced by van Ballegooijen et al. (2011) using the reduced magnetohydrodynamics (RMHD) code called BRAID.

2.2. Including time-dependence and higher dimensions

Previous numerical simulations of reflection-driven RMHD turbulence with the full nonlinear terms include Dmitruk & Matthaeus (2003), Perez & Chandran (2013), and prior studies using BRAID on closed loops (van Ballegooijen et al. 2011; Asgari-Targhi & van Ballegooijen 2012; Asgari-Targhi et al. 2013, 2014). Our version of BRAID uses the three-dimensional equations of RMHD (Strauss 1976; Montgomery 1982; Zank & Matthaeus 1992; Bhattacharjee et al. 1998) to solve for the nonlinear reactions between Alfvén waves generated at the single footpoint of an open flux tube. RMHD relies on the assumption that the incompressible magnetic fluctuations $\delta\mathbf{B}$ in the system are small compared to an overall background field \mathbf{B}_0 . At scales within the turbulence inertial range, observations show that $\delta\mathbf{B}$ is much smaller in amplitude than the strength of the surrounding magnetic field \mathbf{B} and $\delta\mathbf{B}$ is perpendicular to \mathbf{B} (Matthaeus et al. 1990; Tu & Marsch 1995; Chen et al. 2012).

Some implementations of RMHD combine together the implicit assumptions of incompressible fluctuations, high magnetic pressure (i.e., plasma $\beta \ll 1$), and a uniform background field \mathbf{B}_0 . However, the flux tubes we model in the upper chromosphere and low corona have some regions with $\beta \approx 1$ and a vertical field \mathbf{B}_0 that declines rapidly with height. It is not necessarily the case that RMHD applies in this situation. However, it was shown in Section 3.1 of van Ballegooijen et al. (2011) that there is a self-consistent small-parameter expansion that gives rise to a set of RMHD equations appropriate for the chromosphere and corona. In these equations, the dominant, first-order fluctuations are transverse and incompressible—even when $\beta \approx 1$ —and gravitational stratification is included to account for the height variation of \mathbf{B}_0 .

BRAID uses two cross-sectional dimensions of the flux tube and a third dimension along the length of the flux tube, which aligns with the background field B_0 . Alfvén waves are generated at the lower boundary by random footpoint motions with an rms velocity of 1.5 km s⁻¹ and correlation time of 60 s. These fluctuations are generated by taking a randomized white-noise time stream and passing it through a low-pass (Gaussian) frequency filter that removes fluctuations shorter than the specified correlation time. The time stream is normalized to the desired rms velocity amplitude and split up between two orthogonal low- k_\perp Bessel-function modes of the cylindrically symmetric system. The driver modes are shown in Figure 2 and are discussed further in Appendix B of van Ballegooijen et al. (2011).

The magnetic and velocity fluctuations can be approximated by

$$\delta\mathbf{B} = \nabla_\perp h \times \mathbf{B}, \quad (1a)$$

$$\delta\mathbf{v} = \nabla_\perp f \times \hat{\mathbf{B}}, \quad (1b)$$

where \mathbf{B} is the full magnetic field vector, whose magnitude varies with height, and $\hat{\mathbf{B}}$ is the unit vector along the mag-

Table 1
Models in BRAID

Modeled structure	Travel time to $2 R_\odot$	Expansion factor	Speed at 1 AU	Identifier
Polar Coronal Hole	770 s	4.5	720 km s ⁻¹	PCH
Equatorial Streamer	3550 s	9.1	480 km s ⁻¹	EQS
Near Active Region	4400 s	41	450 km s ⁻¹	NAR

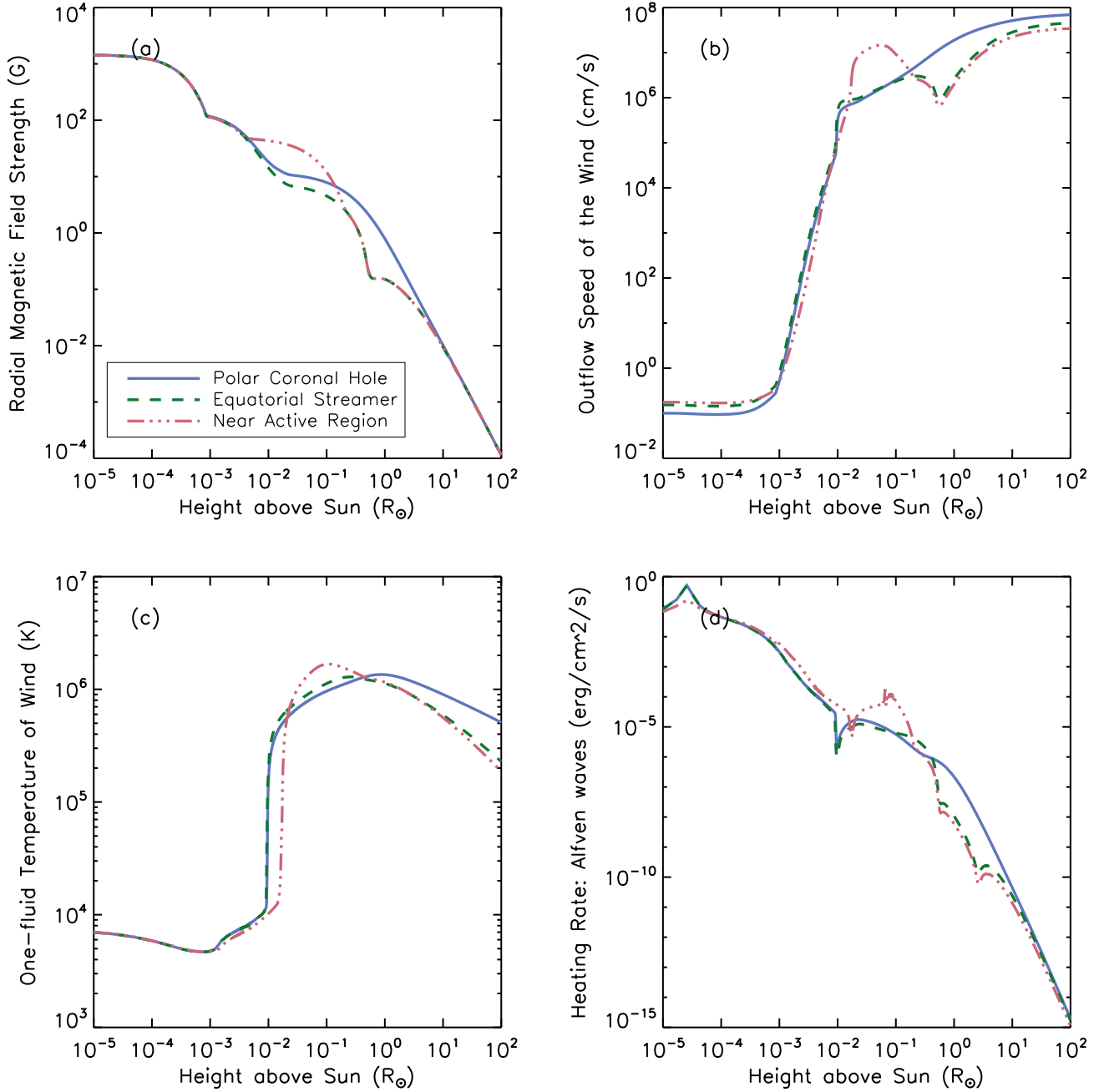


Figure 1. The primary input to ZEPHYR are (a) the magnetic profiles of three representative coronal structures. Results for the bulk solar wind properties from each flux tube include: (b) outflow speed, (c) one-fluid temperature, and (d) Alfvénic heating rate.

netic field. Also, $h(\mathbf{r}, t)$ is a height- and time-dependent function that is analogous to the standard RMHD magnetic flux function, and $f(\mathbf{r}, t)$ is a velocity stream function (sometimes called ψ in other derivations of RMHD). We can also define the magnetic torsion parameter $\alpha \equiv -\nabla_\perp^2 h$ and the parallel

component of vorticity $\omega \equiv -\nabla_\perp^2 f$ (see, e.g., Montgomery 1982). The functions $h(\mathbf{r}, t)$ and $f(\mathbf{r}, t)$ satisfy the coupled

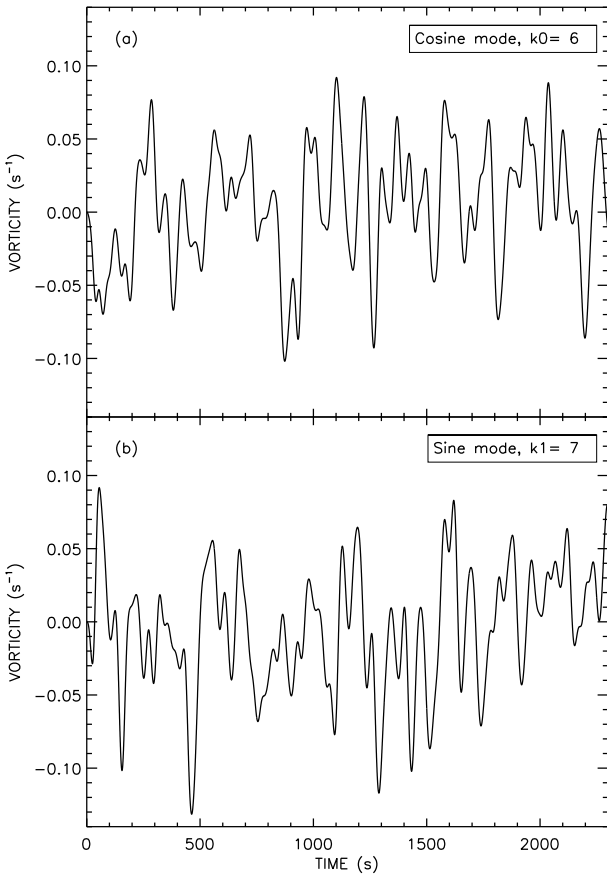


Figure 2. We show here vorticity ω from (a) cosine and (b) sine driver modes for the PCH.

equations

$$\frac{\partial \omega}{\partial t} + \hat{\mathbf{B}} \cdot (\nabla_{\perp} \omega \times \nabla_{\perp} f) = v_A^2 [\hat{\mathbf{B}} \cdot \nabla \alpha + \hat{\mathbf{B}} \cdot (\nabla_{\perp} \alpha \times \nabla_{\perp} h)] + D_v, \quad (2a)$$

$$\frac{\partial h}{\partial t} = \hat{\mathbf{B}} \cdot \nabla f + \frac{f}{H_B} + \hat{\mathbf{B}} \cdot (\nabla_{\perp} f \times \nabla_{\perp} h) + D_m, \quad (2b)$$

where H_B is the magnetic scale length and D_v and D_m describe the effects of viscosity and resistivity (see detailed derivation in van Ballegooijen et al. 2011). Both D_v and D_m have a hyperdiffusive k_{\perp}^4 dependence so that the smallest eddies are damped preferentially and the cascade is allowed to proceed without significant damping over most of the k_{\perp} inertial range.

In this paper, we have extended previous work using BRAID by using an open upper boundary condition instead of a closed coronal loop. The model extends to a height of $z_{\text{top}} = 2R_{\odot}$. This height was chosen to model as much of the solar wind acceleration region as possible, without extending into regions where the wind speed becomes an appreciable fraction of the Alfvén speed, since the RMHD equations of BRAID don't include the outflow speed. To implement the open upper boundary condition, we set ω_+ (which corresponds to the downward Elsässer variable Z_+) to zero, whereas in the previous coronal loop models that used BRAID, it was set to the opposite footpoint's boundary time stream as described

above (Asgari-Targhi et al. 2014, and references therein).

3. TIME-AVERAGED RESULTS FROM THREE MODELED FLUX TUBES

In this paper, we present three models that are representative of common coronal structures (the same from Table 1). Figure 3 gives some of the time-steady background variables for the three models, based on the input magnetic field profiles shown in Figure 1.

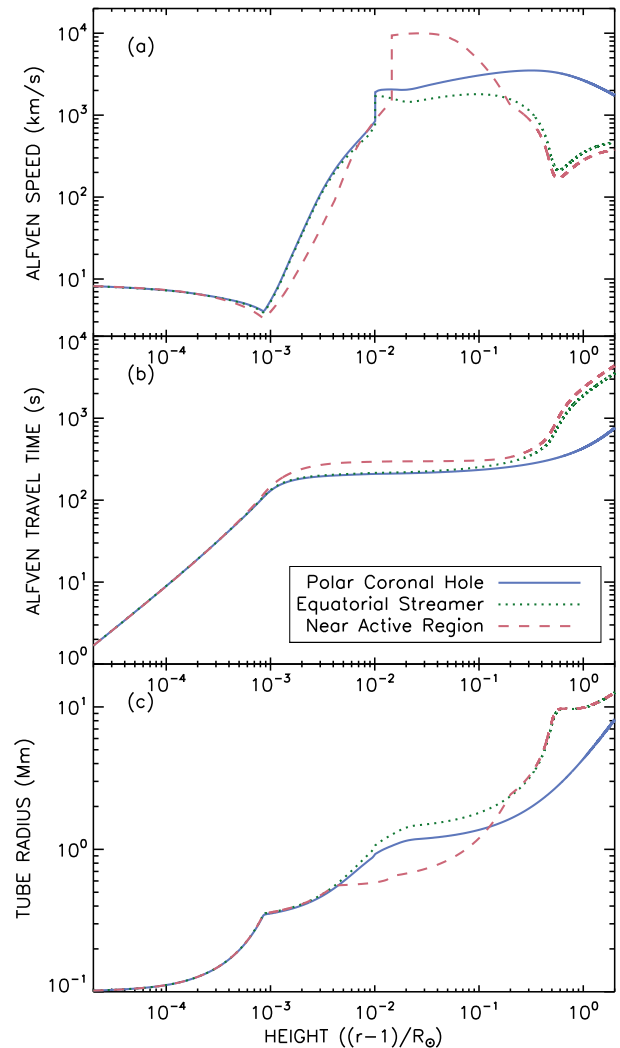


Figure 3. Radial profiles for (a) Alfvén speed, (b) Alfvén travel time, and (c) tube radius.

The Alfvén speed, $V_A = B/\sqrt{4\pi\rho}$ shows a rapid rise in the upper chromosphere, followed by varied behavior in the corona depending on the model. The Alfvén travel time is defined as a monotonically increasing function of height,

$$\tau_A(z) = \int_0^z \frac{dz'}{V_A(z')} \quad (3)$$

where $z=0$ is the photospheric lower boundary of each model. The BRAID code uses τ_A as the primary height coordinate.

Figure 3 shows the modeled transverse radius of the flux tube, which is normalized to 100 km at $z = 0$ (i.e., a typical length scale for an intergranular bright point) and is assumed to remain proportional to $B^{-1/2}$ in accordance with magnetic flux conservation.

Figure 4 provides the time-averaged results from BRAID for the PCH. The transition region is at a travel time of roughly 210 s and is shown with a dotted line. In Figure 4a, we show the magnetic, kinetic, and total energy densities of the RMHD fluctuations. We plot these quantities separately since no equipartition is assumed. Figure 4b shows the increase in the rms transverse velocity amplitude, Δv_{rms} with increasing height, which roughly follows the expected sub-Alfvénic WKB relation $\Delta v_{\text{rms}} \propto \rho_0^{-1/4}$ below the transition region. The heating rate is also broken up into magnetic (from the D_m term), kinetic (from the D_v term), and total for Figure 4c. Finally, we show the magnetic field fluctuation as a function of travel time in Figure 4d. Like the rms velocity, the sub-Alfvénic WKB relation $\Delta b_{\text{rms}} \propto \rho_0^{1/4}$ is followed below the transition region but diverges above it.

The quantities plotted in Figures 4b, 4d, and 5b have gone through two “levels” of root mean square averaging. First, we take the variance over all k_\perp modes at a given height and time, then take the square root. Then, at each height, we take an average over the simulation-time dimension using the squares of the first level of rms values. It is those quantities that we then take the square root of and plot.

In Figure 5a, we show the magnitude of the Elsässer variables, $Z_\pm = \delta \mathbf{v} \pm \delta \mathbf{B} / \sqrt{4\pi\rho_0}$, for the PCH model, and show the fluctuations Δv_{rms} and Δb_{rms} in Figure 5b. Note that here Δb_{rms} is in velocity units, as the actual fluctuations are divided by $\sqrt{4\pi\rho_0}$ (where ρ_0 is the background density) for comparison with the velocity fluctuations. Our boundary condition enforces that the incoming waves (Z_+) have exactly zero amplitude at the upper boundary of our model. Figure 5a also shows the radial dependence of the Elsässer variables from the ZEPHYR model for this coronal hole presented by Cranmer et al. (2007). The ZEPHYR code computes the Alfvénic wave energy using a damped wave action conservation equation that contains the assumption that $Z_- \gg Z_+$. Thus, when reporting the magnitudes of the Elsässer variables here for direct comparison with the BRAID results, we make use of Equation (56) of Cranmer et al. (2007) and correct for non-WKB effects by multiplying these quantities by a factor of $(1 + \mathcal{R}^2)/(1 - \mathcal{R}^2)$, where \mathcal{R} is the reflection coefficient. With this correction, there is good agreement between the modeling of the PCH for both codes. We use the same correcting factor when plotting the Δv_{rms} in Figure 5b. Because ZEPHYR assumes equipartition, Δv_{rms} and Δb_{rms} are equivalent for that model.

Figure 6 shows the Elsässer variables and the amplitudes of magnetic and velocity fluctuations for both the equatorial streamer (EQS) and active region (NAR) models to a height of $z = 0.5R_\odot$, where turbulence has had time to develop in the simulation. It is worthy of note that the NAR model shows an increase in Z_+ above the transition region where the PCH and EQS models show a decrease. For these models in Figure 6b and the results for the PCH (Figure 5b), the shape of the Δb_{rms} is expected to have a sharp increase at the transition region, while the Δv_{rms} doesn’t show it (see, e.g., Figure 9 of Cranmer & van Ballegooijen 2005).

3.1. Energy partitioning in the corona

In our previous modeling using ZEPHYR (see Section 2.1), we assumed equipartition between kinetic and magnetic potential energy densities. With BRAID, we are able to investigate how far the PCH model differs from this simplifying assumption. Figure 7 shows the ratio of the time-averaged magnetic and kinetic energy densities. Above the transition region, equipartition is a valid assumption. However, at the base of the flux tube, magnetic potential energy dominates, and this transitions to a stronger dominance of the kinetic energy right up to the transition region.

Also plotted in Figure 7 are six curves showing predictions from non-WKB reflection with a range of frequencies between 0.7 and 4.0 mHz. While the general shape is consistent with the BRAID results, it is interesting to note that the linear method of computing non-WKB reflection does have its limits. These predictions were made using the coronal hole model from Cranmer & van Ballegooijen (2005) as a basis. However, that model had a lower transition region ($z_{TR} \approx 0.003R_\odot$), so we have multiplied the height coordinate by a factor of 3.4 to match with the ZEPHYR/BRAID coronal hole model used in this project.

Non-WKB theory predicts the kinetic energy to dominate in the chromosphere (e.g., $E_M/E_K < 1$ at low heights). This was discussed in Appendix A of Cranmer & van Ballegooijen (2005) as an after-effect of the transition from kink-mode MHD waves in the photosphere to volume-filling Alfvén waves in the upper chromosphere. At low frequencies, the kink-mode waves are partially evanescent, with two possible solutions for the height-increase of Δv_{rms} . One of the solutions has $E_M/E_K < 1$ and the other has $E_M/E_K > 1$. However, only the solution with $E_M/E_K < 1$ has a physically realistic energy density profile (exponentially decaying with increasing height), and this solution also corresponds to a net upward phase speed (see also Wang et al. 1995).

3.2. Heating rates: comparison with time-steady modeling

We compare the time-averaged heating rates from BRAID with the results from the time-steady modeling using ZEPHYR. Figure 8a shows the radial dependence of the heating rate Q , and Figure 8b shows the ratio between the numerically computed heating rates Q with the phenomenological heating rate Q_{phen} , as well as comparisons between Q and phenomenological heating rates with added correction factors ($Q_{Z,07}$ and Q_{loop}), described in the following paragraphs. The heating rate Q_{phen} is based on the result of a long series of turbulence simulations and models (Dobrowolny et al. 1980; Grappin et al. 1983; Hossain et al. 1995; Matthaeus et al. 1999; Dmitruk et al. 2001, 2002; Chandran et al. 2009). The analytical expression for this base phenomenological rate is given by:

$$Q_{\text{phen}} = \rho_0 \frac{Z_-^2 Z_+ + Z_+^2 Z_-}{4L_\perp} \quad (4)$$

where ρ_0 is the solar wind density, Z_- and Z_+ are the Elsässer variable amplitudes that represent incoming and outgoing Alfvén waves, and L_\perp is the turbulent correlation length. We normalize L_\perp to a value of 75 km at the photosphere (Cranmer et al. 2007). This allows us to write $L_\perp = 0.75R$, where R is the radius of the flux tube, which scales as $B^{-1/2}$. Below the transition region, $Q/Q_{\text{phen}} \approx 0.2$, which is similar to what van Ballegooijen et al. (2011) found for closed loops. Above the transition region, $Q/Q_{\text{phen}} \gg 1$, which may be explainable if the actual correlation length L_\perp expands less rapidly than we assumed from its proportionality with the flux

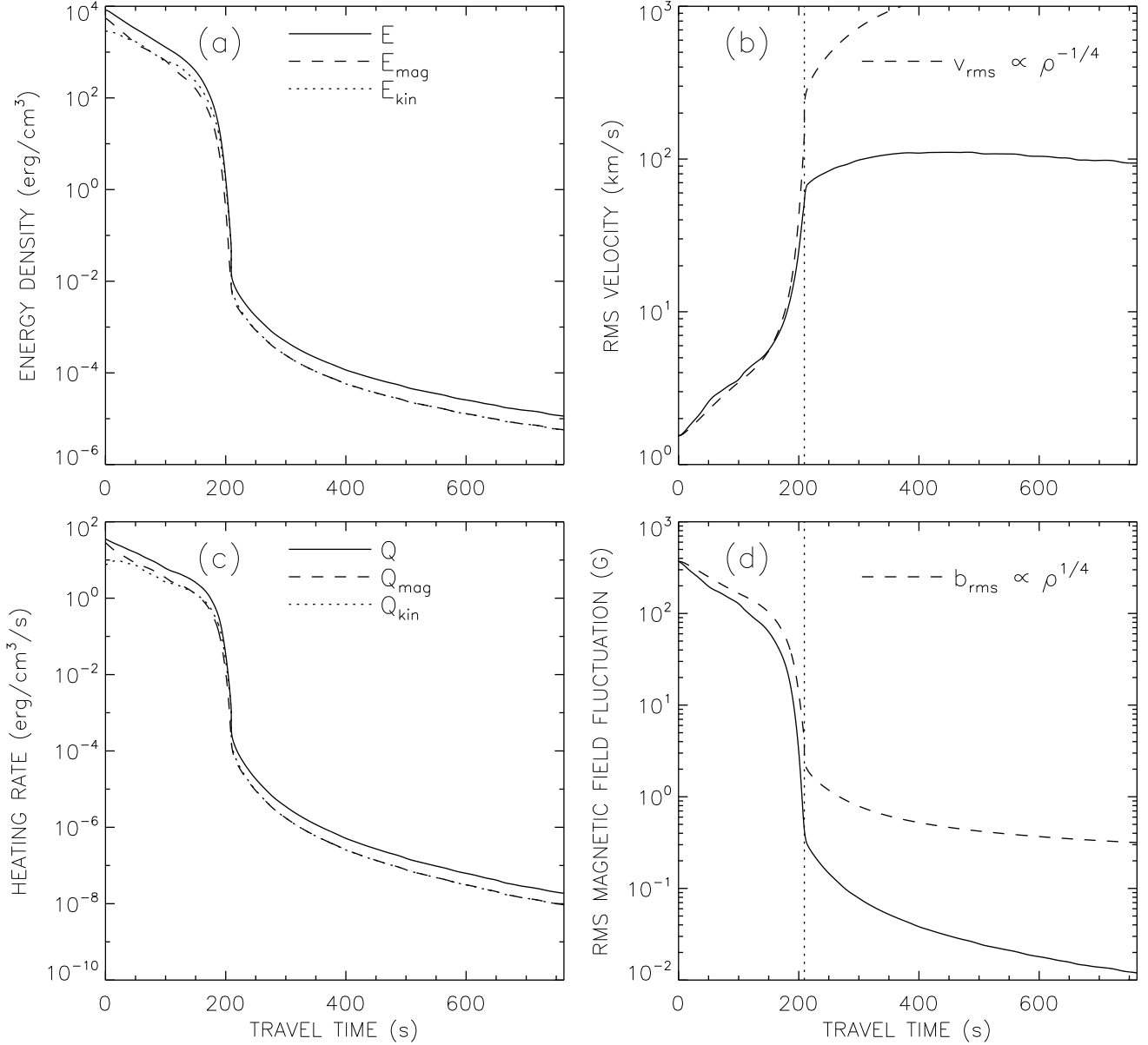


Figure 4. The time-averaged results for the PCH model are shown as a function of Alfvén travel time as a proxy for height above photosphere: (a) Energy density, (b) rms velocity, (c) heating rate, and (d) rms magnetic field fluctuation.

tube radius R . Because the ratio Q/Q_{phen} strays as much as an order of magnitude away from unity, we further compare BRAID's computed heating rate with analytical expressions that contain correcting factors that take into account efficiency of turbulence as a function of height.

The first of the two efficiency factors we use is based on the prior work of [Dmitruk et al. \(2001\)](#), [Dmitruk & Matthaeus \(2003\)](#), and [Cranmer et al. \(2007\)](#). The extended expression, $Q_{Z,07}$ is given by:

$$Q_{Z,07} = \epsilon_{\text{turb}} Q_{\text{phen}}, \quad (5a)$$

$$\epsilon_{\text{turb}} = \frac{1}{1 + (t_{\text{eddy}}/t_{\text{ref}})^n}, \quad (5b)$$

where t_{eddy} is the outer-scale eddy cascade time, $t_{\text{eddy}} = L_{\perp} \sqrt{3\pi}/(1+M_A)/v_{\perp}$, and t_{ref} is the macroscopic Alfvén wave reflection timescale, $t_{\text{ref}} = 1/|\nabla \cdot \mathbf{V}_A|$ ([Cranmer et al. 2007](#)).

In the expression for t_{eddy} , the velocity v_{\perp} is the amplitude of perpendicular fluctuations, defined previously in the BRAID results as Δv_{rms} . When $t_{\text{eddy}} \gg t_{\text{ref}}$, turbulent heating is quenched. The turbulent efficiency factor ϵ_{turb} accounts for regions where energy is carried away before a turbulent cascade can develop. The exponent n is set to 1 based on analytical and numerical models by [Dobrowolny et al. \(1980\)](#), [Matthaeus & Zhou \(1989\)](#), and [Oughton et al. \(2006\)](#). The efficiency factor works to make $Q_{Z,07} < Q_{\text{phen}}$, bringing the ratio $Q/Q_{Z,07}$ up relative to Q/Q_{phen} . At low heights, where the efficiency factor is low, the inclusion of the efficiency factor defined in Equation (5)b does help to bring Q and $Q_{Z,07}$ into better agreement. At large heights, the efficiency factor is closer to 1, so Q_{phen} and $Q_{Z,07}$ both underestimate the heating rate computed by BRAID.

An alternative efficiency factor has emerged from studies

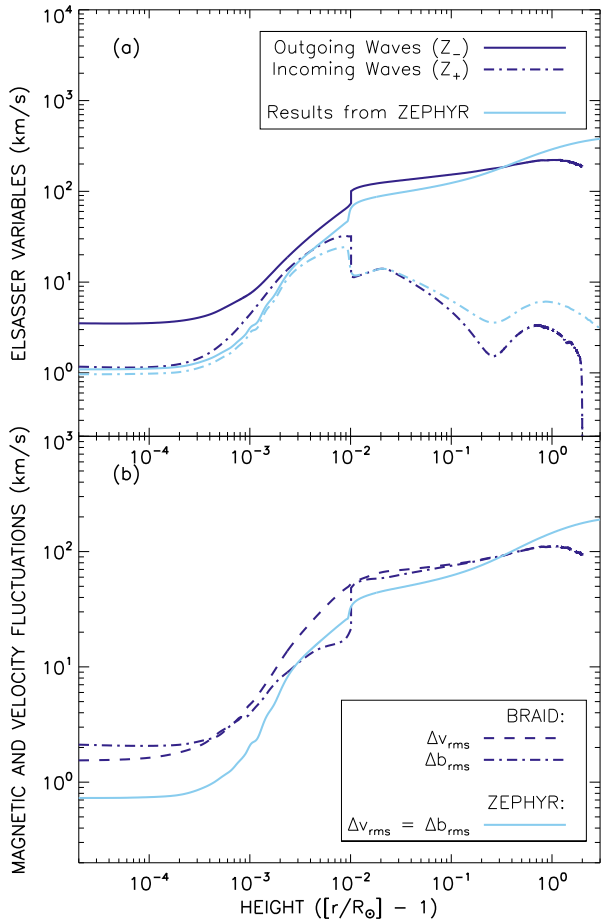


Figure 5. For the PCH model, we show (a) the time-averaged amplitudes of incoming and outgoing Alfvén waves and (b) the rms amplitudes of magnetic and velocity fluctuations from BRAID and ZEPHYR.

of closed coronal loops driven by slow transverse footpoint motions. In such models, magnetic energy is built up from the twisting and shearing motions of the field lines (Parker 1972), and the energy dissipation appears to follow a cascade-like sequence of quasi-steady relaxation events. Cranmer (2009) parametrized the time-averaged heating rate in these models as

$$Q_{\text{loop}} = \epsilon_{\text{loop}} Q_{\text{phen}}, \quad \epsilon_{\text{loop}} = \left(\frac{L_{\perp} V_A}{v_{\perp} L_{\parallel}} \right)^{\alpha} \quad (6)$$

where L_{\parallel} is often defined as the “loop length” for closed magnetic structures, and α is an exponent that describes the sub-diffusive nature of the cascade in a line-tied loop. The quantity in parentheses is a ratio of timescales; this ratio is the nonlinear time over the wave travel time. To set the value of L_{\parallel} in our open-field models, we follow Schrijver et al. (2004), who found that open and closed regions can be modeled using a unified empirical heating parametrization when the actual loop length L is replaced by an effective length scale

$$L_{\parallel} \approx \frac{L}{1 + (L/L_0)} \quad (7)$$

where $L_0 = 50$ Mm. Thus, for open-field regions in which $L \gg$

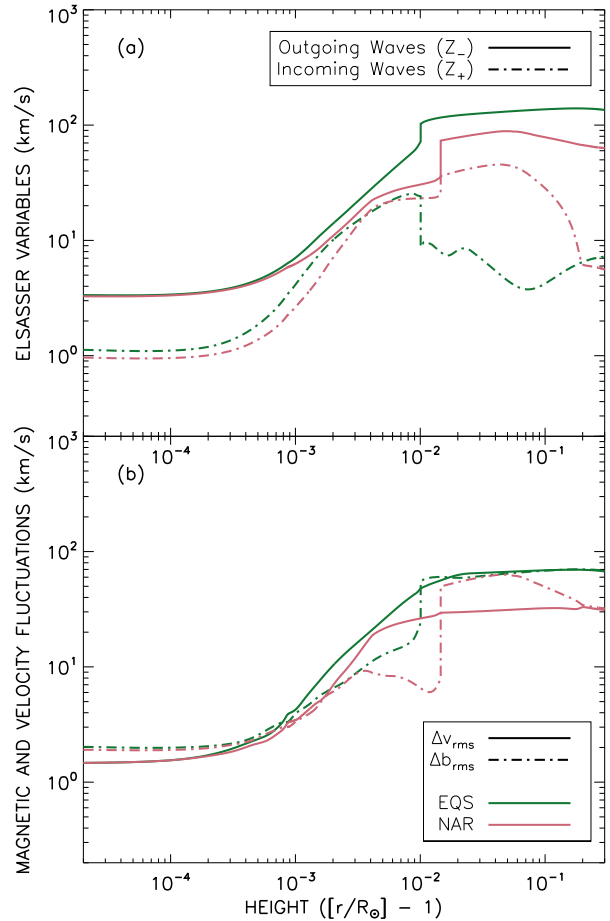


Figure 6. Similar to Figure 5; For the EQS and NAR models, we show the (a) outgoing and incoming Elsässer variables and (b) the rms amplitudes of magnetic and velocity fluctuations.

L_0 , we use $L_{\parallel} = L_0$.

The exponent α describes how interactions between counter-propagating Alfvén wave packets can become modified by MHD processes such as scale-dependent dynamic alignment (Boldyrev et al. 2009). The value $\alpha = 0$ corresponds to a classical hydrodynamic cascade. Gomez et al. (2000) constructed a model of MHD turbulence in which $\alpha = 1.5$, and van Ballegooijen (1986) constructed a random-walk type model in which $\alpha = 2$ (see also van Ballegooijen & Cranmer 2008). Rappazzo et al. (2008), however, found from numerical simulations that α can occupy any value between 1.5 and 2, depending on the properties of the background corona and wave driving. Cranmer (2009) created an analytic prescription for specifying α in a way that agrees with the Rappazzo et al. (2008) results. Subsequently, Cranmer (2009) and Cranmer et al. (2013b) found that when modeling the coronal X-ray emission from low-mass stars, the longest loops—which seem to be most appropriate to compare with open-field regions—tend to approach the high end of the allowed range of exponents (i.e., $\alpha \approx 2$). Thus, in this paper we use $\alpha = 2$ and note that the differences between Q_{loop} and Q_{phen} will be reduced for smaller values of the exponent. At the largest heights, Q_{loop} better matches the BRAID numerical

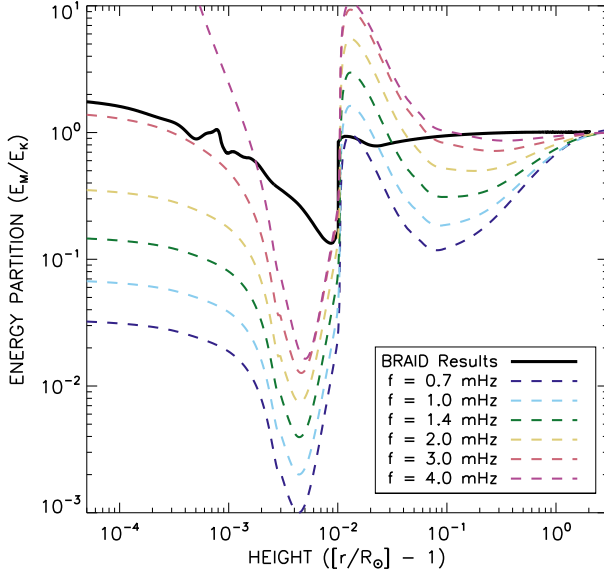


Figure 7. Ratio of magnetic to kinetic energy density differs from equipartition below the transition region.

results than either Q_{phen} or $Q_{Z,07}$.

For additional comparison, in Figure 9 we plot the ratio of BRAID numerical results with the phenomenological heating rate for all three of our flux tube models. The behavior of the heating rate expressions with efficiency factors is similar, so we show only the ratio Q/Q_{phen} in Figure 9. Note that the EQS model behaves similarly to the PCH model, but the NAR model exhibits a marked decrease in the ratio Q/Q_{phen} in the low corona before increasing again to approach the EQS model at the top of the grid. This behavior is reminiscent of the closed-field models of van Ballegooijen et al. (2011), in which Q/Q_{phen} came back down to values of 0.2–0.3 in the coronal part of the modeled loops.

4. EXTENDED ANALYSIS OF TIME VARIABILITY

4.1. Statistical variations as a source of multithermal plasma

The turbulent heating simulated by BRAID was found by van Ballegooijen et al. (2011) to be quite intermittent and variable on small scales. Figure 10 illustrates some of this variability by showing the fluctuation energy density and heating rate volume-averaged over the low corona (i.e., between the transition region at $z=0.01 R_\odot$ and an upper height of $0.5 R_\odot$). This is a similar plot as Figure 4 of van Ballegooijen et al. (2011). Even with this substantial degree of spatial averaging, the nanoflare-like burstiness generated by the turbulence is evident in Figure 10. There is a large body of prior work concerning such intermittent aspects of turbulent heating (see, e.g., Einaudi et al. 1996; Hendrix & van Hoven 1996; Dmitruk & Gómez 1997; Dmitruk et al. 1998; Einaudi & Velli 1999).

The time-varying heating rate should also give rise to a similarly variable coronal temperature structure. We investigate the possibility that the resulting stochastic distribution of temperatures may be partially responsible for the observational signatures of *multithermal* plasmas—e.g., nonzero widths of the differential emission measure (DEM) distribution. Asgari-Targhi & van Ballegooijen (2012) studied the spatial and temporal response of a conduction-dominated corona to the simulated variations in Q from BRAID. They found that con-

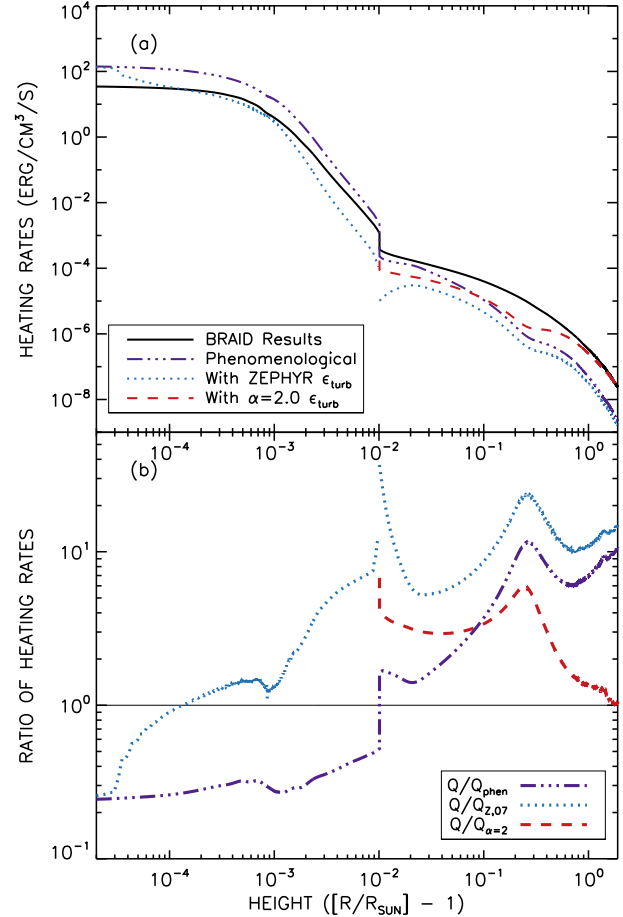


Figure 8. We compare the time-averaged heating rate from BRAID for the PCH model with the phenomenological expressions given by Equations (4), (5) and (6) by (a) directly plotting them as a function of height and (b) plotting ratios of the rates, with a thin black line showing unity.

duction leads to a “smeared out” temperature structure that nevertheless retains much of the bursty variability seen in the heating rate. Here, we perform an even simpler estimate of the distribution of temperatures by taking the distribution of volume-averaged heating rates $\langle Q \rangle$ shown in Figure 10 and processing each value through the simple conductive scaling relation of Rosner et al. (1978). Thus,

$$\frac{\langle T \rangle}{\langle \bar{T} \rangle} = \left(\frac{\langle Q \rangle}{\langle \bar{Q} \rangle} \right)^{2/7} \quad (8)$$

where $\langle T \rangle$ is an estimated volume-averaged coronal temperature. The normalizing value of the heating rate $\langle \bar{Q} \rangle$ is assumed to be the mean value of $\langle Q \rangle$ seen in the BRAID simulation. For simplicity, we take the normalizing value of the temperature $\langle \bar{T} \rangle$ to be the maximum coronal temperature found in the corresponding ZEPHYR model from Cranmer et al. (2007). The PCH, EQS, and NAR models exhibited values of $\langle \bar{T} \rangle$ of 1.352, 1.224, and 1.675 MK, respectively.

Figure 11(a) shows the distribution of derived values of $\langle T \rangle$ for the PCH model. If the temperatures along this flux tube were measured by standard ultraviolet and X-ray diagnostics, with time integrations long in comparison to the scale of vari-

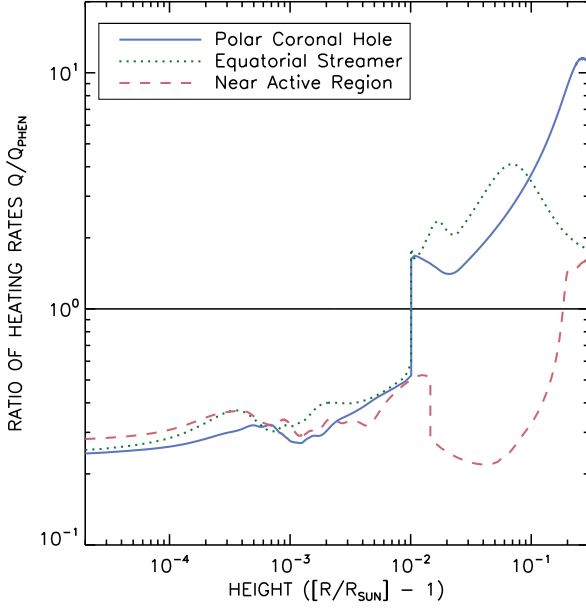


Figure 9. For each model, we show the ratio of the time-averaged heating rate from BRAID with the phenomenological expression given by Equations (4).

ability in the BRAID model, then this distribution would be equivalent to the DEM. For each simulated DEM, we measured its representative “width” in the same way as described by Schmelz et al. (2014); i.e., we used the points at which the DEM declined to 0.1 times its maximum value. For the PCH, EQS, and NAR models, we found widths of 0.2294, 0.2259, and 0.2839 in units of “dex” ($\log T$), respectively.

Figure 11(b) compares the properties of the three simulated DEMs with a selection of observationally derived coronal-loop DEMs from Schmelz et al. (2014). The BRAID models do appear to reproduce the observed multithermal nature of coronal plasmas, both in the absolute values of the widths (which fall comfortably within the range of the observed values) and in the overall trend for hotter models to have broader DEMs. Of course, the open-field models studied here only span a very limited range of central temperatures $\langle T \rangle$ in comparison to the observed cases.

4.2. Power spectrum of fluctuations

For the PCH model, we investigated in detail the power spectrum of the velocity fluctuations caused by the Alfvén waves. To generate the Fourier transform, we assumed constant time spacing using the model results spanning from $t = \tau_A$ to $t = 2\tau_A$. We subtracted the mean, doubled the length to make a periodic sequence, and then fed the cleaned quantity into a traditional FFT procedure. The power spectrum is the product of the result of that FFT procedure with its complex conjugate. This procedure gives us these spectra at each height z .

In Figure 12, we examine a contour plot of the power in these fluctuations. Certain frequencies in the 10^{-2} Hz to $10^{-1.5}$ Hz range have a relatively high amount of power at all heights, while at the higher frequencies, there is an increase in power as a function of height. This is more easily seen in Figure 13. We show the basal input spectrum with a dashed line, and the power spectrum at the upper boundary of our model lies above the power spectrum at the photospheric base for

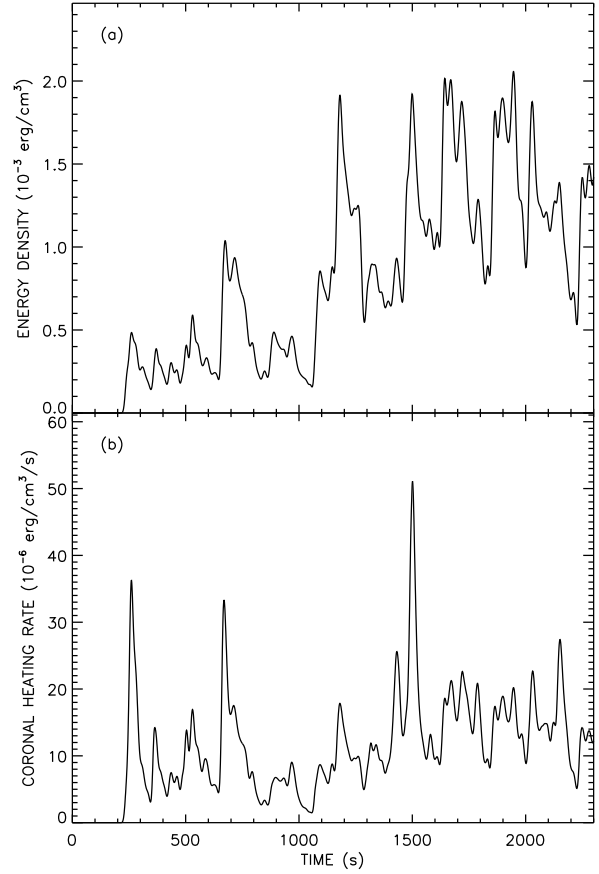


Figure 10. Due to the random jostling that generates the Alfvén waves, the (a) spatially-averaged energy density in the corona and (b) spatially-averaged heating rate per unit volume in the corona are bursty and strongly time-dependent in nature.

the highest frequencies. Both boundaries show that there is a boost above the input spectrum for high frequencies.

Figure 13 shows that the high-frequency part of the BRAID turbulent power spectrum appears to be a power law $\mathcal{P} \propto f^{-n}$, where the value of n varies a bit with height in the model. Looking only at the FFT data with $f \geq 0.03$ Hz, we found that $n \approx 4.5$ at the photospheric base, and then it steepens at larger heights to take on values of order 5.2–6.4 (i.e., a mean value of 5.8 with a standard deviation of ± 0.6) at chromospheric heights below the TR. In the corona, however, n decreases a bit to a mean value of 4.9 and a smaller standard deviation of ± 0.3 . Some of the quoted standard deviations are likely due to fitting uncertainties of the inherently noisy power spectra, but it is clear that the corona exhibits less variation in n than the regions below the TR.

Despite several decades of spacecraft observations of power-law frequency spectra in the turbulent solar wind, it was not immediately obvious that the BRAID power spectrum should have exhibited such power-law behavior. Spacecraft-frame measurements are often interpreted as being a spatial sample through quasi-stationary wavenumber variations (see, e.g., Taylor 1938; Horbury et al. 2012). In strong-field MHD turbulence, the dominant wavenumber cascade is expected to be in the k_\perp direction. However, the Alfvénic fluctuations that make up an MHD cascade have a dispersion relation in

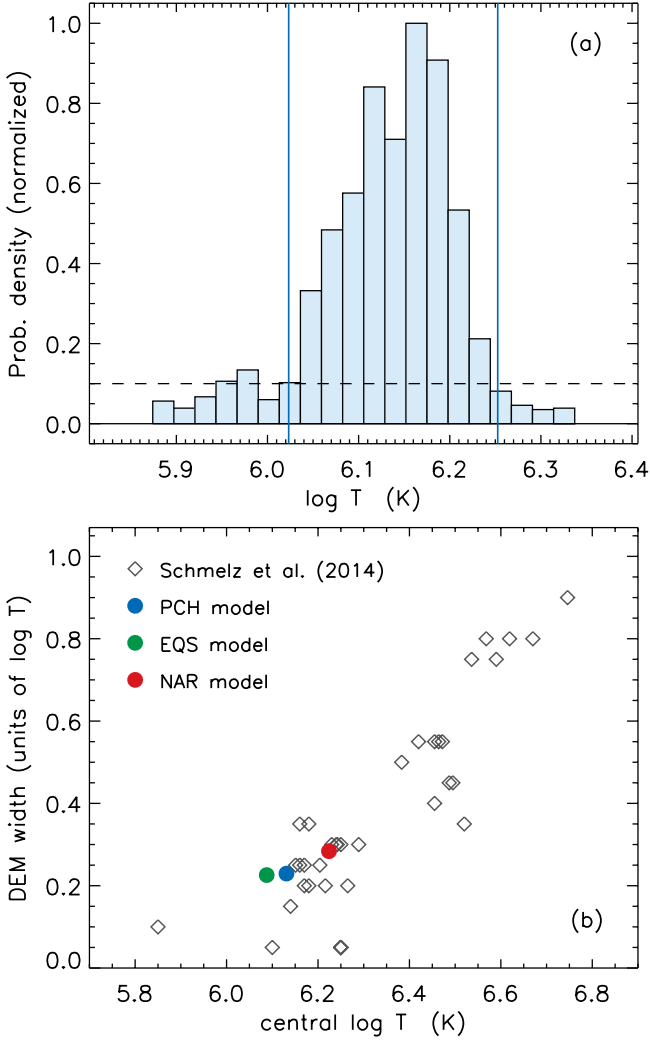


Figure 11. (a) Scaled histogram of the probability distribution of coronal temperatures estimated from BRAID heating rates. Temperatures at which the distribution drops to 0.1 times the maximum value (dashed line) are indicated by solid red lines. (b) Observed DEM widths from Schmelz et al. (2014), plotted as the relative width in $\log T$ space and computed from the reported number of $\log T$ “bins” (gray diamonds), compared with simulated DEM widths from the PCH (red circle), EQS (green circle), and NAR (blue circle) models.

which the frequency depends primarily on k_{\parallel} . Thus, MHD (especially RMHD) turbulence is typically described as “low-frequency turbulence” and the idea of an inherent power-law *frequency cascade* is met—usually, rightly so—with skepticism.

There has been one proposed model in which a power-law spectrum in frequency (i.e., in k_{\parallel}) occurs naturally and without the need for substantial parallel cascade: the so-called “critical balance” model of Goldreich & Sridhar (1995). In this picture, strong mixing is proposed to occur between the turbulent eddies (primarily moving perpendicular to the background field) and Alfvén wave packets (moving parallel to the field), such that the parameter space “filled” by a fully developed cascade is determined by the critical balance parameter

$$\chi = \frac{k_{\parallel} V_A}{k_{\perp} v_{\perp}} \quad (9)$$

taking on values $\chi \lesssim 1$ (see also Higdon 1984). The limit

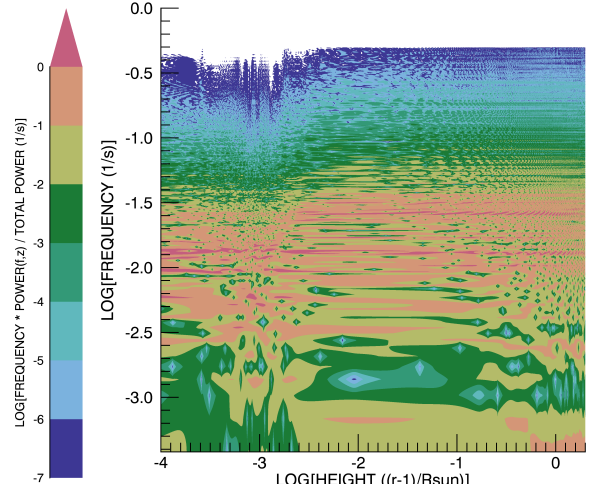


Figure 12. Contour plot of the power spectrum in the PCH model showing power in color, as a function of height and of frequency.

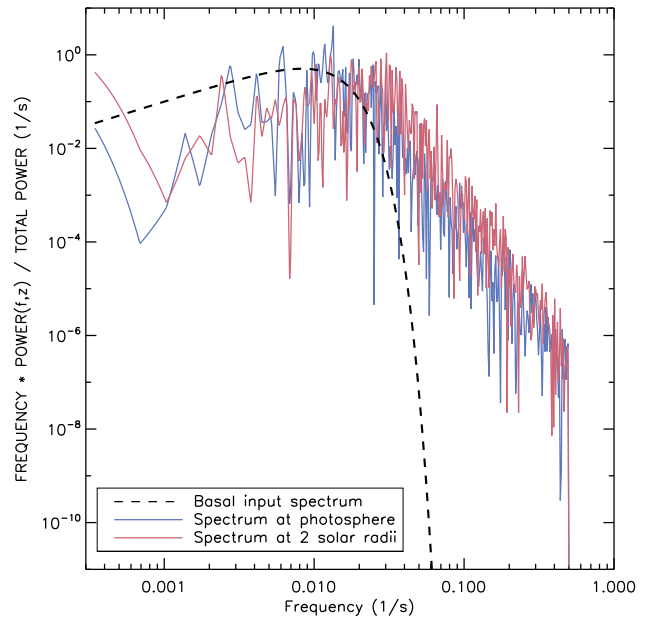


Figure 13. Power spectra for the upper and lower boundaries of the PCH model compared to the input spectrum show a boost in power at high frequencies.

$\chi \ll 1$ corresponds generally to low-frequency fluctuations with $k_{\parallel} \ll k_{\perp}$ as is expected in anisotropic MHD turbulence. This parameter can also be interpreted as a ratio of timescales.

Following the implications of critical balance led Goldreich & Sridhar (1995) to a phenomenological expression of the time-steady inertial range, given here as

$$E(k_{\parallel}, k_{\perp}) = \frac{V_A v_{\perp}(k_{\perp})}{k_{\perp}^3} g(\chi) \quad (10)$$

where this combines Equations (5) and (7) of Goldreich & Sridhar (1995). Above, E is a three-dimensional power spectrum that gives the magnetic energy density variance (in velocity-squared units) when integrated over the full volume

of wavenumber space,

$$\frac{\langle B_{\perp}^2 \rangle}{8\pi\rho} = \int d^3\mathbf{k} E(k_{\parallel}, k_{\perp}) = \int df \mathcal{P}(f), \quad (11)$$

and we also define the frequency spectrum $\mathcal{P}(f)$ in a similar way. Note that $2\pi f = \omega = k_{\parallel} V_A$ in the local rest frame of the plasma under the assumption that the fluctuations are Alfvén waves.

In Equation (10) above, $v_{\perp}(k_{\perp})$ is the reduced velocity spectrum, which specifies the magnitude of the velocity perturbation at length scales k_{\perp}^{-1} and k_{\parallel}^{-1} . This spectrum is often assumed to be a power-law with $v_{\perp} \propto k_{\perp}^{-m}$. The exponent m has been proposed to range between values of 1/3 (strong turbulence; Goldreich & Sridhar 1995) and 1/2 (weak turbulence; Galtier et al. 2000). Lastly, the function $g(\chi)$ in Equation (10) is a “parallel decay” function that is expected to become negligibly small for $\chi \gg 1$. Because $g(\chi)$ is normalized to unity when integrated over all χ , a simple approximation for it is a step function,

$$g(\chi) \approx \begin{cases} 1, & \chi \leq 1, \\ 0, & \chi > 1 \end{cases} \quad (12)$$

(see also Cho et al. 2002; Cranmer & van Ballegooijen 2012). The above form for $g(\chi)$, combined with the assumption that the reduced spectrum $v_{\perp}(k_{\perp})$ extends out to $k_{\perp} \rightarrow \infty$, leads to the high-frequency end of the frequency spectrum obeying a power law, with

$$\mathcal{P}(f) \propto f^{(m+1)/(m-1)}. \quad (13)$$

The strong turbulence case ($m = 1/3$, $\mathcal{P} \propto f^{-2}$) has been studied extensively both observationally and theoretically (see, e.g., Horbury et al. 2012).

Of course, the BRAID models highlighted in this paper do *not* have reduced perpendicular velocity spectra that extend over large ranges of k_{\perp} space. The models presented here (similar to those of van Ballegooijen et al. (2011)) resolve only about one order of magnitude worth of an “inertial range” in k_{\perp} space. For the step-function version of $g(\chi)$ given above, the imposition of a $v_{\perp}(k_{\perp})$ cutoff above an arbitrary k_{\max} produces a frequency spectrum $\mathcal{P}(f)$ that is similarly cut off above a frequency f_{\max} determined by critical balance ($\chi = 1$) at $k_{\perp} = k_{\max}$.

In an alternative to the step-function version of $g(\chi)$, Cranmer & van Ballegooijen (2003) found an analytic solution for $g(\chi)$ by applying an anisotropic cascade model that obeyed a specific kind of advection–diffusion equation in three-dimensional wavenumber space. The general form of $g(\chi)$ is reminiscent of a suprathermal kappa function (see, e.g., Pierrehumbert & Lazar 2010), which is roughly Gaussian at low χ and a power-law at large χ . For $\chi \gg 1$, Cranmer & van Ballegooijen (2003) found that $g(\chi) \propto \chi^{-(3+s)/2}$, where s is the ratio of the model’s perpendicular advection coefficient to the perpendicular diffusion coefficient. It is still not known if MHD turbulence in the solar corona and solar wind exhibits a universal value of s , or even whether or not s is even a physically meaningful parameter. Nevertheless, the wavenumber diffusion framework of Zhou & Matthaeus (1990) and Matthaeus et al. (2009) has been shown to be consistent with a value of $s = 2$ in this family of advection–diffusion equations. In a different model of coronal turbulence, van Ballegooijen (1986) showed that a cascade of slow random-walk displacements of the field lines can be treated as the case $s = 1$. On the basis

of observations alone, Cranmer & van Ballegooijen (2003) and Landi & Cranmer (2009) found that if s could be maintained at small values of order 0.1–0.3, there would be sufficient high-frequency wave energy to heat protons and minor ions via ion cyclotron resonance.

No matter the value of s or the reduced spectral index m , it can be shown that at large frequencies ($f > f_{\max}$), a power law of the form $g(\chi) \propto \chi^{-n}$ produces a power-law frequency spectrum $\mathcal{P} \propto f^{-n}$ with the same exponent (see the integration over k_{\perp} in Equation (11)). Thus, we postulate that measuring n from the BRAID simulations *may* be a way to extract information about the exponent s , with

$$s = \frac{2n-4}{3}. \quad (14)$$

The values of n reported above imply a photospheric value of $s \approx 1.7$, which increases to $s \approx 2.5$ in the chromosphere (with a relatively large spread) and then decreases to $s \approx 1.9$ in the corona. The similarities to the theoretical value of $s = 2$ (from, e.g., Zhou & Matthaeus 1990; Matthaeus et al. 2009) are suggestive, but not conclusive.

4.3. Nanoflare statistics of heating rate variability

We investigated the variability of heating and energy as a function of height and time throughout the simulation. In a given finite “zone,” the energy lost via dissipative heating can be calculated using the heating rate as

$$E(z, t) = Q(z, t)\Delta z(\pi R^2)\Delta t, \quad (15)$$

where the zones are defined at a set of heights, z , with unequal spacing Δz , and at a set of times, t , with equal spacing $\Delta t = 0.25$ s. In Figure 14, we provide a contour plot of the energy, comparable with Figure 6b of Asgari-Targhi et al. (2013). Many of the impulsive heating events that result in spikes of energy over a short time frame stop at the transition region, which lies at $0.01R_{\odot}$, but some extend to ten times that height. There is also a lack of energy at the beginning of the simulation ($t < \tau_A$), where the information has not yet had time to propagate up through the model grid.

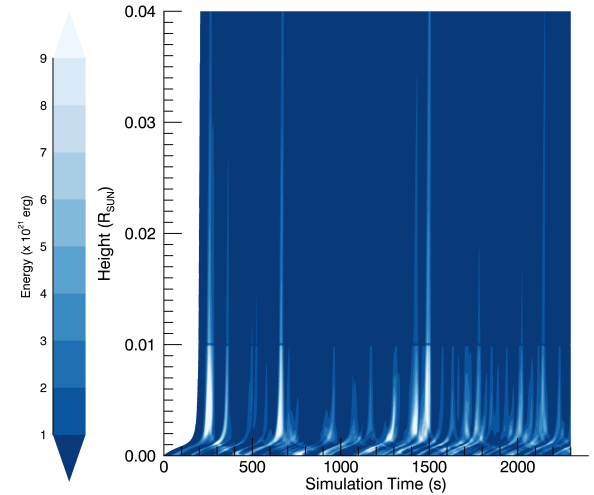


Figure 14. Dependence of energy on height above photosphere (y-axis) and time (x-axis). The transition region is at $0.01 R_{\odot}$.

Following the method of Asgari-Targhi et al. (2013), we then use box capturing to get a statistical sense of the distri-

bution of energy in these zones throughout the corona. In order to be directly comparable to their defined events, we also use boxes with a width of 19.4 seconds in simulation time and height of 19.4 seconds in Alfvén travel time (a proxy for height). This choice in box size results initially in 118 sections across the time dimension and 39 sections along the height dimension. However, the lowest 10 boxes are at heights below the transition region, and we plot only boxes in the corona in Figure 15. Additionally, we take out the first 770 seconds corresponding to one Alfvén travel time in the PCH model (recall Table I and Equation (3)) to ensure that the waves have had time to propagate fully throughout the corona.

These cuts result in 78 time sections and 29 height sections, giving us a total of 2262 coronal boxes. The arithmetic mean in log-space of the energy contained within these boxes is 21.91 with a standard deviation of 0.97. The average energy contained in the boxes is lower than that found by Asgari-Targhi et al. (2013), since our model does not have two strong footpoints supplying separate sources of counter-propagating Alfvén waves, but it is still a significant amount of energy. Figure 15 also shows that we find a few events that reach higher energies than the histogram from Asgari-Targhi et al. (2013), and that higher tail gets well into the classical nanoflare expected energies (Hannah et al. 2011). The minimum-energy event contains $10^{19.04}$ erg while the maximum-energy event contains $10^{24.97}$ erg. It is worthy of note that the peak energies captured in these boxes fall well within the “picoflare” range (Axford et al. 1999; Parnell & Jupp 2000). All of these events are a natural product of the total heating coming out of BRAID, suggesting that the physics contained within these models may lead to the formation of pico- and nanoflares.

5. DISCUSSION AND CONCLUSIONS

We have analyzed three typical open magnetic field structures using one-dimensional time-steady modeling and three-dimensional time-dependent RMHD modeling. These structures represent characteristic flux tubes anchored within a polar coronal hole, on the edge of an equatorial streamer, and neighboring a strong closed-field active region. We show that the time-averaged properties of the higher-dimensional BRAID models agree well with that of the less-computationally-expensive ZEPHYR models.

We looked in detail at the energy partitioning, as BRAID imposes no assumptions or restrictions. At heights above the transition region, equipartition is shown to work well to describe the results from BRAID, and is assumed in the ZEPHYR algorithm. We also compared the energy partitioning with predictions from non-WKB reflection for a range of frequencies, showing the limitations of the linear method for such predictions. The time-averaged heating rates from BRAID are lower than the phenomenological expression in Equation (5) for the heating rate below the transition region, rising sharply toward the upper boundary.

In BRAID, Alfvén waves are generated by random footpoint motions, whose properties and driving modes are described in Section 2.2. As the Alfvén waves propagate upward from the photosphere to the open upper boundary at a height of 2 solar radii, they partially reflect and cause turbulence to develop. With the time-dependence included in BRAID, we are able to show the bursty nature of turbulent heating by Alfvén waves. We show that this heating brings energy up into the corona and provide a statistical distribution of energy per event. The more energetic events (i.e., boxes

with the most energy) fall within expected nanoflare values.

Overall, we show that time-steady modeling does a good job of predicting the time-averaged results from time-dependent modeling. There is, however, a bounty of information that can be found only by looking at changes in the heating rate over time. Moving from one dimension to three allows the model to contain more realistic physics. We have shown that these models of typical magnetic field structures provide additional compelling evidence to support the idea that Alfvén-wave-driven turbulence heats the corona and accelerates the solar wind.

ACKNOWLEDGMENTS

This material is based upon work supported by the National Science Foundation Graduate Research Fellowship under Grant No. DGE-1144152 and by the NSF SHINE program under Grant No. AGS-1259519. L.N.W. also thanks the Harvard Astronomy Department for the student travel grant and Loomis fund. The authors gratefully acknowledge Adriaan van Ballegooijen for many keen insights and for the development of the BRAID model. The authors also thank the anonymous reviewer for their helpful comments and suggestions.

REFERENCES

- Arge, C. N., & Pizzo, V. J. 2000, *J. Geophys. Res.*, 105, 10465
- Asgari-Targhi, M., & van Ballegooijen, A. A. 2012, *ApJ*, 746, 81
- Asgari-Targhi, M., van Ballegooijen, A. A., Cranmer, S. R., & DeLuca, E. E. 2013, *ApJ*, 773, 111
- Asgari-Targhi, M., van Ballegooijen, A. A., & Imada, S. 2014, *ApJ*, 786, 28
- Axford, W. I., McKenzie, J. F., Sukhorukova, G. V., et al. 1999, *Space Sci. Rev.*, 87, 25
- Banaszkiewicz, M., Axford, W. I., & McKenzie, J. F. 1998, *A&A*, 337, 940
- Bhattacharjee, A., Ng, C. S., & Spangler, S. R. 1998, *ApJ*, 494, 409
- Boldyrev, S., Mason, J., & Cattaneo, F. 2009, *ApJ*, 699, L39
- Chandran, B. D. G., Dennis, T. J., Quataert, E., & Bale, S. D. 2011, *ApJ*, 743, 197
- Chandran, B. D. G., Quataert, E., Howes, G. G., Hollweg, J. V., & Dorland, W. 2009, *ApJ*, 701, 652
- Chen, C. H. K., Mallet, A., Schekochihin, A. A., et al. 2012, *ApJ*, 758, 120
- Cho, J., Lazarian, A., & Vishniac, E. T. 2002, *ApJ*, 564, 291
- Cranmer, S. R. 2009, *ApJ*, 706, 824
- Cranmer, S. R., Asgari-Targhi, M., Miralles, M. P., et al. 2015, *Phil. Trans. Royal Soc. A*, 373, 20140148
- Cranmer, S. R., & van Ballegooijen, A. A. 2003, *ApJ*, 594, 573
- . 2005, *ApJS*, 156, 265
- . 2012, *ApJ*, 754, 92
- Cranmer, S. R., van Ballegooijen, A. A., & Edgar, R. J. 2007, *ApJS*, 171, 520
- Cranmer, S. R., van Ballegooijen, A. A., & Woolsey, L. N. 2013a, *ApJ*, 767, 125
- Cranmer, S. R., Wilner, D. J., & MacGregor, M. A. 2013b, *ApJ*, 772, 149
- Dmitruk, P., & Gómez, D. O. 1997, *ApJ*, 484, L83
- Dmitruk, P., Gómez, D. O., & DeLuca, E. E. 1998, *ApJ*, 505, 974
- Dmitruk, P., & Matthaeus, W. H. 2003, *ApJ*, 597, 1097
- Dmitruk, P., Matthaeus, W. H., Milano, L. J., et al. 2002, *ApJ*, 575, 571
- Dmitruk, P., Milano, L. J., & Matthaeus, W. H. 2001, *ApJ*, 548, 482
- Dobrowolny, M., Mangeney, A., & Veltri, P. 1980, *Physical Review Letters*, 45, 144
- Einaudi, G., & Velli, M. 1999, *Physics of Plasmas*, 6, 4146
- Einaudi, G., Velli, M., Politano, H., & Pouquet, A. 1996, *ApJ*, 457, L113
- Galtier, S., Nazarenko, S. V., Newell, A. C., & Pouquet, A. 2000, *Journal of Plasma Physics*, 63, 447
- Goldreich, P., & Sridhar, S. 1995, *ApJ*, 438, 763
- Gomez, D. O., Dmitruk, P. A., & Milano, L. J. 2000, *Sol. Phys.*, 195, 299
- Grappin, R., Leorat, J., & Pouquet, A. 1983, *A&A*, 126, 51
- Hannah, I. G., Hudson, H. S., Battaglia, M., et al. 2011, *Space Sci. Rev.*, 159, 263
- Hendrix, D. L., & van Hoven, G. 1996, *ApJ*, 467, 887

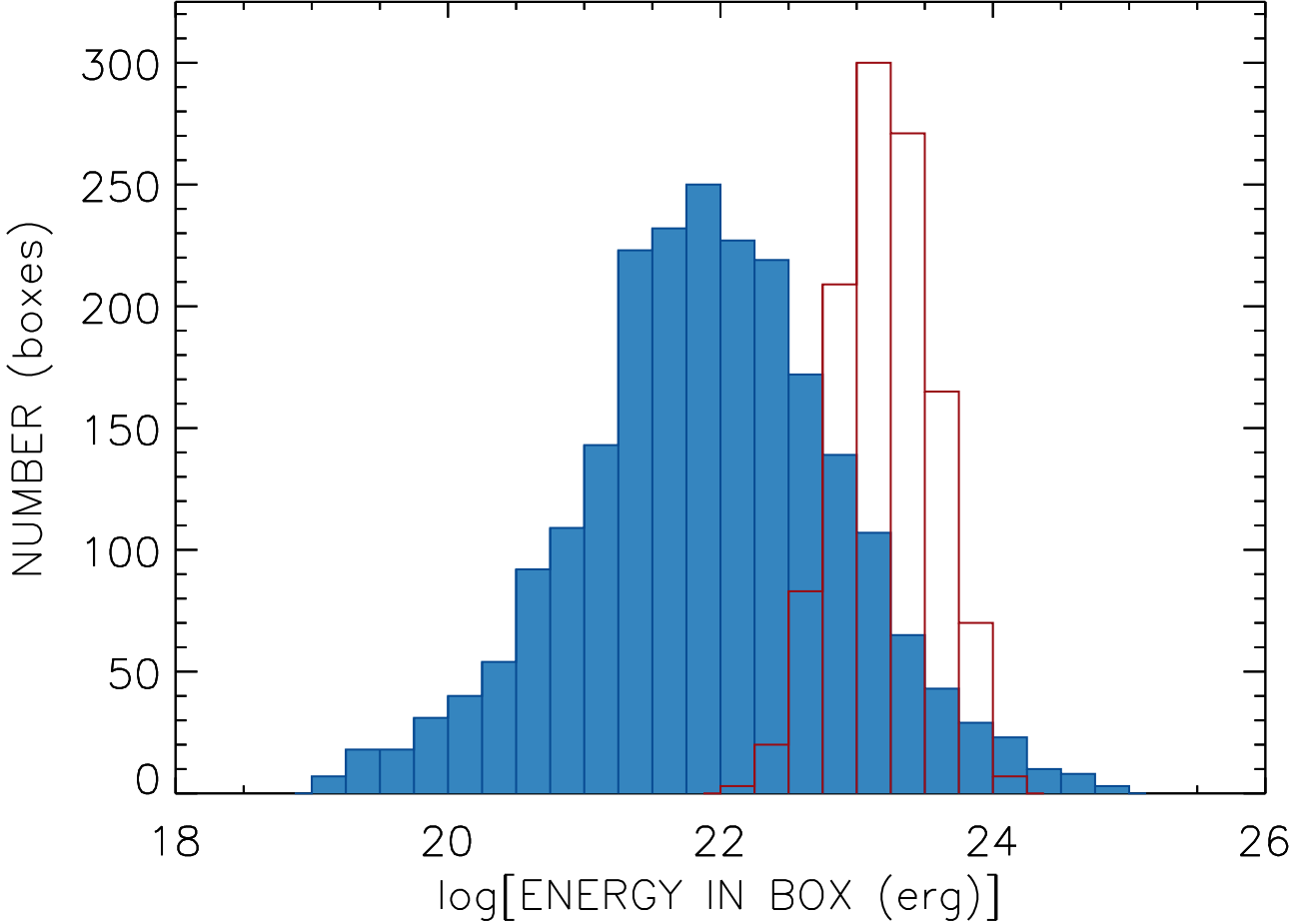


Figure 15. Filled histogram shows the statistical distribution of energy contained in boxes of space and time for the PCH model. Only boxes above the transition region are used. For comparison, red outlined histogram shows the results from closed magnetic loops (Asgari-Targhi et al. 2013).

- Higdon, J. C. 1984, ApJ, 285, 109
 Hollweg, J. V. 1986, J. Geophys. Res., 91, 4111
 Horbury, T. S., Wicks, R. T., & Chen, C. H. K. 2012, Space Sci. Rev., 172, 325
 Hossain, M., Gray, P. C., Pontius, Jr., D. H., Matthaeus, W. H., & Oughton, S. 1995, Physics of Fluids, 7, 2886
 Klimchuk, J. A. 2015, Phil. Trans. Royal Soc. A, 373, 20140256
 Landi, E., & Cranmer, S. R. 2009, ApJ, 691, 794
 Lionello, R., Velli, M., Downs, C., et al. 2014, ApJ, 784, 120
 Lithwick, Y., Goldreich, P., & Sridhar, S. 2007, ApJ, 655, 269
 Matsumoto, T., & Suzuki, T. K. 2014, MNRAS, 440, 971
 Matthaeus, W. H., Goldstein, M. L., & Roberts, D. A. 1990, J. Geophys. Res., 95, 20673
 Matthaeus, W. H., Oughton, S., & Zhou, Y. 2009, Phys. Rev. E, 79, 035401
 Matthaeus, W. H., Zank, G. P., Oughton, S., Mullan, D. J., & Dmitruk, P. 1999, ApJ, 523, L93
 Matthaeus, W. H., & Zhou, Y. 1989, Physics of Fluids B, 1, 1929
 McIntosh, S. W. 2012, Space Sci. Rev., 172, 69
 Montgomery, D. 1982, Physica Scripta Volume T, 2, 83
 Ofman, L. 2010, Living Reviews in Solar Physics, 7, 4
 Oughton, S., Dmitruk, P., & Matthaeus, W. H. 2006, Physics of Plasmas, 13, 042306
 Oughton, S., Matthaeus, W. H., Wan, M., & Osman, K. T. 2015, Phil. Trans. Royal Soc. A, 373, 20140152
 Parker, E. N. 1972, ApJ, 174, 499
 Parnell, C. E., & De Moortel, I. 2012, Phil. Trans. Royal Soc. A, 370, 3217
 Parnell, C. E., & Jupp, P. E. 2000, ApJ, 529, 554
 Perez, J. C., & Chandran, B. D. G. 2013, ApJ, 776, 124
 Pierrard, V., & Lazar, M. 2010, Sol. Phys., 267, 153
 Rappazzo, A. F., Velli, M., Einaudi, G., & Dahlburg, R. B. 2008, ApJ, 677, 1348
 Rosner, R., Tucker, W. H., & Vaiana, G. S. 1978, ApJ, 220, 643
 Schmelz, J. T., Pathak, S., Brooks, D. H., Christian, G. M., & Dhaliwal, R. S. 2014, ApJ, 795, 171
 Schrijver, C. J., Sandman, A. W., Aschwanden, M. J., & De Rosa, M. L. 2004, ApJ, 615, 512
 Strauss, H. R. 1976, Physics of Fluids, 19, 134
 Suzuki, T. K., & Inutsuka, S.-I. 2006, J. Geophys. Res., 111, 6101
 Taylor, G. I. 1938, Royal Soc. Proceedings Series A, 164, 476
 Tu, C.-Y., & Marsch, E. 1995, Space Sci. Rev., 73, 1
 van Ballegooijen, A. A. 1986, ApJ, 311, 1001
 van Ballegooijen, A. A., Asgari-Targhi, M., Cranmer, S. R., & DeLuca, E. E. 2011, ApJ, 736, 3
 van Ballegooijen, A. A., & Cranmer, S. R. 2008, ApJ, 682, 644
 Verdini, A., Velli, M., Matthaeus, W. H., Oughton, S., & Dmitruk, P. 2010, ApJ, 708, L116
 Wang, Y.-M., & Sheeley, Jr., N. R. 1990, ApJ, 355, 726
 Wang, Z., Ulrich, R. K., & Coroniti, F. V. 1995, ApJ, 444, 879
 Woosley, L. N., & Cranmer, S. R. 2014, ApJ, 787, 160
 Zank, G. P., & Matthaeus, W. H. 1992, Journal of Plasma Physics, 48, 85
 Zhou, Y., & Matthaeus, W. H. 1990, J. Geophys. Res., 95, 14881